Enhancing Molten Tin Methane Pyrolysis Performance for Hydrogen and Carbon Production in a Hybrid Solar/Electric Bubbling Reactor

Malek Msheik, Sylvain Rodat, Stéphane Abanades

Enhancing Molten Tin Methane Pyrolysis Performance for Hydrogen and Carbon Production in a Hybrid Solar/Electric Bubbling Reactor

Malek Msheik, Sylvain Rodat, Stéphane Abanades*

Processes, Materials and Solar Energy Laboratory, PROMES-CNRS, 7 Rue du Four Solaire, 66120 Font Romeu, France

*Correspondence: stephane.abanades@promes.cnrs.fr; Tel.: +33-(0)4-68-30-77-30

Abstract

Methane pyrolysis in liquid metals is a worth-developing process for CO_2-free hydrogen production. This study investigates methane pyrolysis in molten tin and highlights the impact of several parameters on methane conversion (X_{CH4}) in a novel hybrid solar/electric bubbling reactor. Temperature (1200-1300 °C), total inlet gas flow rate (Q_0 = 0.25-0.5 NL/min), melt height (H_{im} = 60-120-235 mm) and hybridization are addressed. Increasing the temperature from 1200 °C to 1300 °C (Q_0 = 0.25 NL/min and H_{im} = 120 mm) improves X_{CH4} (32% vs. 69%). Increasing Q_0 from 0.25 to 0.5 NL/min (T = 1200 °C and H_{im} = 120 mm) reduces X_{CH4} (19% vs. 9%). Doubling the melt height, H_{im} (60 to 120 mm) increases the residence time of bubbles, which increases X_{CH4} (7% vs. 19%). A customized sparger is also tested and shows little effect, probably because the holes are relatively large (1 mm diameter). An immersed bed of steel particles (0.2-0.4 mm diameter) instead shows good results (X_{CH4} = 32%) at a relatively low temperature (1100 °C). Continuous reactor operation at 1300 °C without clogging is also confirmed. Analysis of carbon accumulated at melt surface during molten media methane pyrolysis reveals a tin-containing sheet-like structure.

Keywords: Methane pyrolysis, molten tin, turquoise hydrogen, liquid metal bubble column, sheet-like carbon, hybrid solar/electric reactor.

1 Introduction

In the 21st century, the development of renewable and/or environmentally friendly energy sources to mitigate climate change has known vital progress. For instance, hydrogen is increasingly contributing to the zero-emission scenario projected in 2050. Clean hydrogen production could avoid 60 Gt of CO_2 emissions between 2021 and 2050 [1].

Hydrogen is fundamental in many industrial applications: ammonia and methanol production, oil refining, fuel cells for electricity production, etc. The path to producing hydrogen is the main pillar to fulfill the environmental aspect. Currently, most of the hydrogen demand worldwide (e.g., 90 Mt in 2020) is supplied through CO_2-emitting processes including steam methane reforming (SMR) (48%), partial oxidation of hydrocarbons (30%), and coal gasification (18%) [2]. CO_2 capture and sequestration (CCS) as a potential solution to reduce emissions, shows several drawbacks: the lack of efficiency for long-term storage, the need of depositories in unpopulated areas, not to mention the increase of the production cost (0.67-1.52 €/kg of H_2 without CCS vs. 1.14-2 €/kg of H_2 with CCS) [3]. On the other side, although electrolysis produces green hydrogen, it is still a costly process unable to replace SMR and gasification in the short term (3.04-7.32 €/kg of H_2) [1].

Alternatively, the decarbonization of methane through pyrolysis is drawing attention since it only results in hydrogen gas and solid carbon (Eq. (1)) [4–7]. Such an endothermic reaction has an advantage over SMR and gasification with zero emissions derived from the chemical reaction. Moreover, integrating solar energy for heating makes the whole process environmentally friendly [8]. Methane pyrolysis was mainly conducted in gas-phase media (i.e., an empty reactor that could contain solid catalysts if the process is catalyzed) where reactor clogging and catalyst coking were common issues [6,9–11]. Recently, methane pyrolysis was conducted in bubble columns with molten metals/salts therein [12]. Bubbling methane in a hot molten metal was proposed for the first time in 1931 [13]. When methane is bubbled in a hot liquid medium: (i) the heat transfer from the liquid bulk toward bubbles might be improved compared to an empty reactor [14], (ii) carbon particles, produced as a byproduct, float on the surface of the bath due to the difference of density and hence no clogging occurs, (iii) the liquid medium, if catalytic, does not easily undergo deactivation since carbon is lifted away toward the melt surface.

$$\mathrm{CH_{4(g)}} \rightarrow 2\mathrm{H_{2(g)}} + \mathrm{C_{(s)}} \qquad \Delta \mathrm{H^{\circ}_{25\,^{\circ}C}} = 74.85\ \mathrm{kJ/mol\ of\ CH_4} \tag{1}$$

Such a new path for methane pyrolysis has not been thoroughly investigated yet, especially under solar heating. Most previous studies tested molten metals as liquid media because metals are considered better than salts in terms of catalytic activity. Among the most interesting results, Upham et al. found that $Ni_{0.27}Bi_{0.73}$ had the best catalytic activity among a diversity of metal alloys. Palmer et al. claimed that $Cu_{0.45}Bi_{0.55}$ surpassed $Ni_{0.27}Bi_{0.73}$ despite the weaker intrinsic catalytic performance of Cu compared to Ni. Likewise, Zeng et al. [15] found that tellurium was better than $Ni_{0.27}Bi_{0.73}$. However, Te is very expensive and rare. Gallium was tested by Leal Perez et al. [16] with the use of a 0.2 mm gas sparger, which resulted in a high methane conversion (91% at 1119 °C). Mg showed high catalytic activity at only 700 °C (X_{CH4} = 30%) [17]. Molten tin was also investigated since it has a significantly low melting temperature (232 °C) but it was always reported as a very poor catalyst [18–21]. However, when tin was used with a 0.5 µm gas sparger, there was almost 51% methane conversion at only 750 °C. Such a result could be attributed to the great improvement in terms of heat and mass transfer due to the high gas-tin contact surface [20]. The effect of spargers was also addressed in the work of Kim et al. [22], with a homemade ceramic sparger made from zirconia balls fixed around the outlet of the injector using zirconia paste. The sparger helped to generate small bubbles (0.5 mm) compared to (3-8 mm) when using a normal tube and hence boosted methane

conversion from 15 to 97% in molten $Ni_{0.2}Sn_{0.8}$ (wt.%) alloy. Scheiblehner et al. [23] investigated few metals and copper alloys as molten media for methane pyrolysis. After one hour of operation, they found that $Cu_{0.2}Bi_{0.8}$ resulted in the highest methane conversion (68.44%) followed by Bi (67.42%), $Cu_{0.5}Ni_{0.5}$ (55.75%), Sn (45.39%), $Cu_{0.2}Sn_{0.8}$ (41.18%), $Cu_{0.975}Ga_{0.025}$ (37.22%) and finally Cu (33.46%).

Salts are less common than metals for methane cracking in molten media, probably due to their lower performance in terms of catalysis. They also display lower density resulting in less efficient carbon separation; however, the purification of salt-contaminated carbon is easier than metal-contaminated carbon thanks to possible water flushing. Kang et al. [24] compared a salt mixture of $KCl/MnCl_2$ (67:33 mol%) to each of them when used pure. They claimed that the salt mixture had the best performance with 55% methane conversion at 1050 °C. In another study, they investigated the effect of Fe addition to NaCl or KCl salt. They found that adding 3 wt% Fe to the salt decreased the activation energy of the reaction from 301 to 171 kJ/mol CH_4. Mixture of $MnCl_2$/KCl was also studied by Bae et al. [25] and showed better activity than pure $MnCl_2$ followed by $MnCl_2$/NaCl, $MnCl_2$/LiCl and finally pure KCl. $MnCl_2$/KCl mixture improved the hydrogen selectivity to 99% and reduced the activation energy to 152 kJ/mol compared to 172 kJ/mol for pure $MnCl_2$. Parkinson et al. studied different salts: KCl, KBr, NaCl, NaBr, and a eutectic mixture of NaBr/KBr (48.7:51.3 mol%). KBr resulted in the highest methane conversion (6.22%) at 1000 °C. Rahimi et al. [26] were the first to use a two-phase molten medium consisting of a metal alloy Ni-Bi overlaid by a molten salt (KBr or NaBr). Their study showed that the upper salt phase helped to condense the metal vapor, which resulted in a much metal-free carbon (83 wt% vs. 5 wt% metal contamination without and with salt, respectively). Patzschke et al. [27] examined various solid catalysts dispersed in a eutectic molten salt NaBr/KBr (48.7:51.3 mol%). They reported that Co-Mn showed the best results with high resistance against deactivation.

Along with hydrogen, solid carbon derived from methane cracking in molten media could be interesting for different applications, such as inks, pigments, zinc carbon batteries, stove polish and mostly for tire and synthetic rubber manufacturing (≈75% of current carbon output) [28,29]. The carbon market is growing (12 Mt in 2014 vs. 16.4 Mt in 2022), with most of the increasing demand in China and India. However, methane pyrolysis, if industrialized, may swamp the market with solid carbon (345 Mt /year if all the H_2 is produced through pyrolysis) [12]. Other carbon markets should be developed such as those related to graphitic carbon [3,22]. Its valorization could help to reduce the hydrogen production cost, thus making methane cracking competitive with SMR. As the solid carbon floats on the surface of the liquid medium, it should be continuously separated to warrant process continuity at industrial scale. Some works proposed methods to remove the floating carbon. To separate the carbon periodically, Kudinov et al. [30] proposed inserting a floating structure in the reactor to detect the surface level. Above a certain limit, the accumulated carbon should be removed, by turning on the vacuum to collect the deposit in a tank. Von Wald et al. [31] stated that the accumulated carbon could be removed by entrainment in the outlet gas and then separated through a cyclone. To ensure complete carbon removal, a filter bag can be placed downstream to remove fine particles.

In this study, solar methane pyrolysis in molten tin was investigated since it melts at a low temperature, which simplifies the process. A hybrid solar/electric tubular reactor was designed and built at PROMES-CNRS for this purpose and the influence of several key operating parameters was unraveled. The main performance metrics including gas product composition, methane conversion, hydrogen and carbon yields, and carbon product characteristics were assessed, and the different influencing factors affecting methane pyrolysis were also discussed. Through several experiments,

the effects of various parameters on methane conversion were studied: heating temperature, height of molten tin, feeder orifice design (bubble diameter), inlet gas flow rate, and hybrid heating (electric vs. simultaneous electric and solar heating). As mentioned previously, one of the advantages of methane cracking in molten media is carbon flotation (due to density difference with liquid metals), which begets better resistance to clogging. In this context, two long-term experiments were conducted to check this feature. Carbon byproduct recovered at the liquid metal surface was finally characterized by SEM-EDX and XRD. This study demonstrates for the first time the potential of a hybrid solar-electric reactor for methane pyrolysis in molten media as a promising route toward clean hydrogen and carbon production, and further highlights possible key parameters and strategies to improve the process performance.

2 Solar tubular reactor

2.1 Overall description

The solar tubular reactor was designed and installed at PROMES-CNRS (France) for solar methane cracking experiments (Figure 1). It consists of two concentric alumina tubes, insulated with 70 mm thick circular layers made of polycrystalline mullite/alumina wool and special inorganic fibers and binders. The outer tube was 500 mm long with 23 mm and 30 mm as inner and outer diameters, respectively. The upper part of the outermost tube was maintained with a water-cooled metallic piece made of stainless steel that ensures the cooling of the seal and quenching of outlet gas.

In the lower part of the reactor (zoomed on the right side of Figure 1), there is an electric heater, with a 15 mm height built-in insulation, beneath and atop an 85 mm long coil. Then, a 25 mm height insulation layer separates the top of the heater and a 50 mm high solar cavity with an aperture of 15 mm diameter. The solar energy is concentrated via a 1.5 kW heliostat-parabola system ($\Phi_{parabola} \approx 2$ m with a maximal concentration ratio of 15000). Six thermocouples (T1- T5, type S) and (T6, type K) were set at different locations as shown in Figure 1, to record the temperature along the heated zone. T2 (denoted by T_{elec}) is the reference temperature for the electrically heated zone, while the average of T4 and T5 (denoted by T_{solar}) is the reference temperature of the solar cavity. The temperature of the melt was actually very close to the wall temperature (T_{elec} and T_{solar}) since liquid tin has a high thermal conductivity, as verified in a previous work [32].

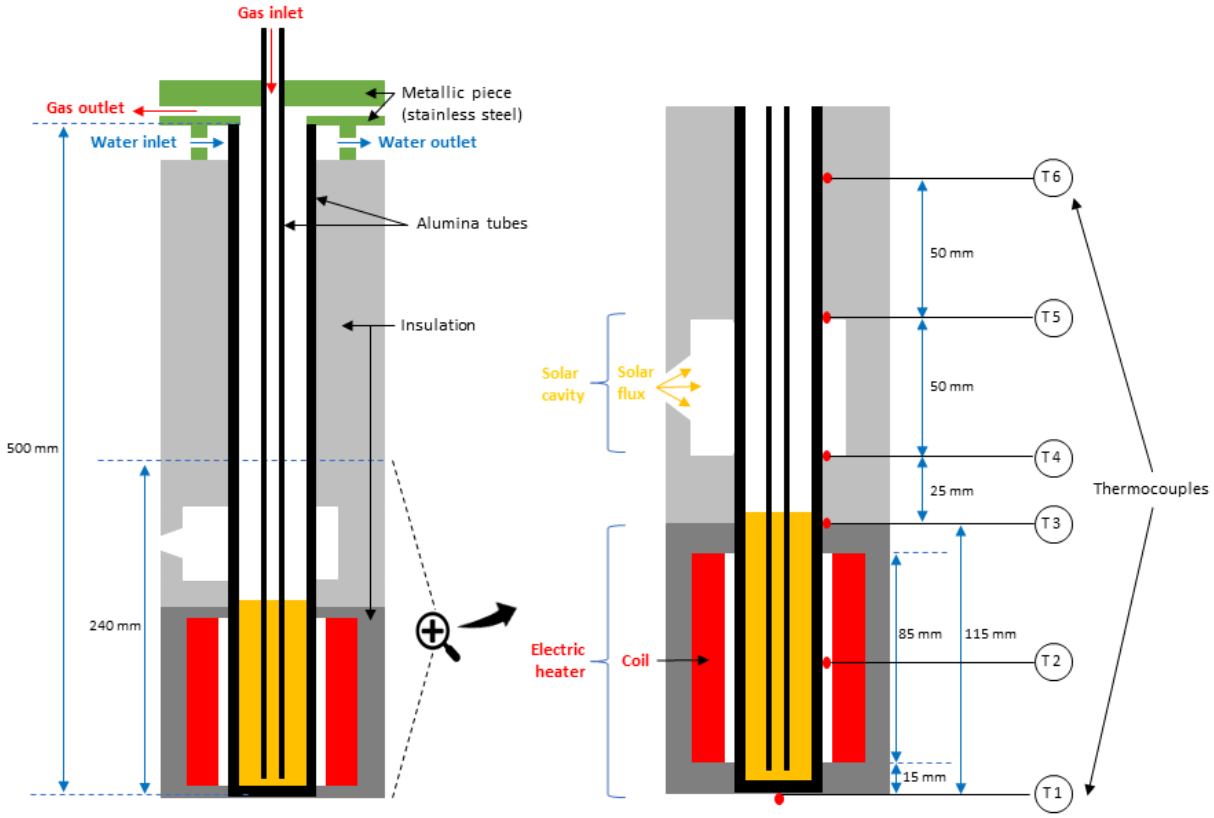

Figure 1: Solar tubular reactor scheme (the right side is a zoom on the lower part of the reactor)

2.2 Gas feeder design

To study the effect of the orifice design on methane decomposition, two different feeders were used. Both were made of alumina with 700 mm total length, and 3 mm and 6 mm as inner and outer diameters, respectively (Figure 2a&b). The first tube was open-end (Figure 2a), while the second was closed-end, drilled with a total of 9 holes, each of 1 mm diameter located on three different heights (Figure 2b).

The bottom of the orifice in Figure 2a was always kept 10 mm above the bottom of the outer tube. As the drilled feeder had a closed end, it was put in contact with the bottom of the outer tube, so that its three upmost holes could likewise be 10 mm above the bottom of the outer tube (Figure 2b).

The main difference between these feeders was the orifice design which might affect the bubble size. Theoretically, smaller orifices should generate smaller bubbles and hence improve heat and mass transfer between liquid and gas, and consequently, favor methane decomposition.

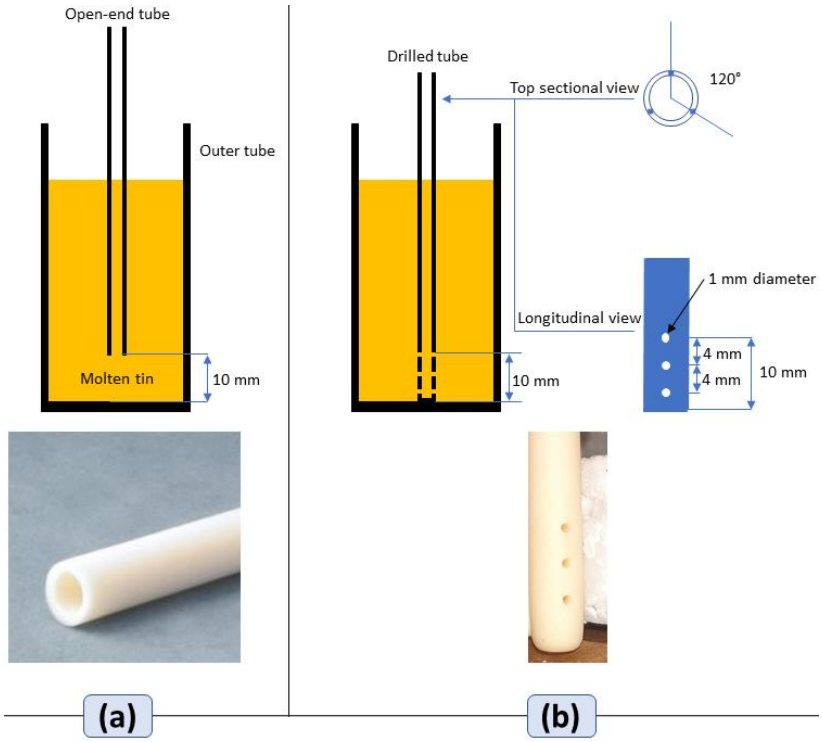

Figure 2: Orifice design of two different feeders: schematic representations with pictures underneath. (a) Open-end alumina tube, (b) Side-drilled alumina tube

2.3 Process flow diagram

This section describes the process setup including operator command and data acquisition (Figure 3). Methane and argon flow rates were controlled through mass flowmeters (Brooks SLA5850S), the solar heating through an adjustable shutter and the electric heating through electrical power. The pressure of the gas entering and exiting the reactor was monitored by pressure indicators (Keller Druckmesstechnik PAA-23, 0-3 bar) and controlled by relief valves (Swagelok SS-RL3S6MM).

The exiting gas mixture was carbon-filtered through two cartridge gas filters (Classic filters SG231.221, 0.1 µm particles removal) in series with a water bubbler to capture eventual condensable gases. The purified gas was sent to a gas analyzer (Rosemount NGA 2000 MLT3) and to a gas chromatograph (Varian CP 4900, equipped with two channels: MolSieve 5 Å PLOT for H_2 and CH_4, PoraPLOT U for H_2, CH_4, and C_2H_y) to measure the mole fractions of gas components. All these data along with pressures, temperatures and DNI (Direct Normal Irradiance) were registered on a PC for subsequent analysis.

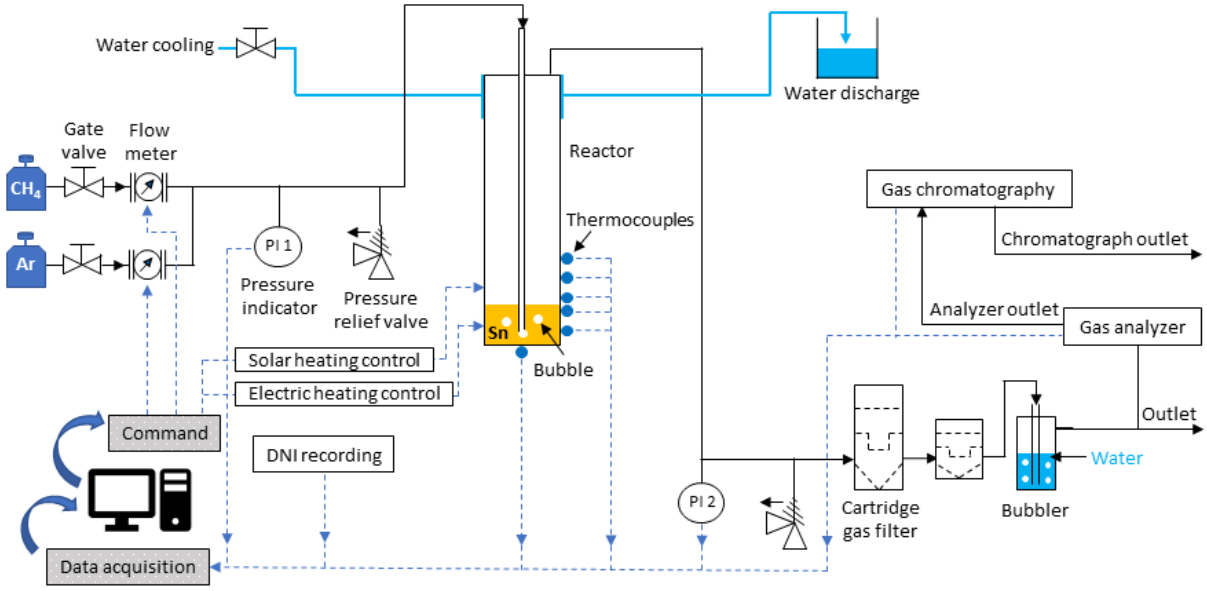

Figure 3: Process setup for methane cracking experiments

2.4 Materials and Methods

CH_4 and Ar were both purchased from Air Liquide (France) with 99.9% and 99.99% purity, respectively. Tin was used as a liquid medium thanks to its physical properties (melting temperature = 232 °C, boiling temperature = 2602 °C), allowing easy processing in methane cracking applications (1000-1400 °C). The amount of tin required to form a specific bath of a certain height was calculated according to the equation of tin density function of the operating temperature [33]. For instance, 308 g were weighed when the required tin height was 120 mm at 1000 °C.

At the beginning of experiments, the reactor was purged with argon to drive off oxygen. Then, tin granules were progressively inserted in the outer tube and were melted under electric heating. When tin became liquid, the injector was descended to match the design illustrated in Figure 2 based on the used feeder.

2.4.1 Performance indicators

Methane conversion, hydrogen and carbon yields, were calculated using (Eq. (2), (3) and (4)), respectively [32]:

$$X_{CH_4} = 1 - \frac{y_{CH_4}.F_t}{F_{0,CH4}} \quad (2)$$

$$Y_{H_2} = \frac{y_{H_2}.F_t}{2F_{0,CH_4}} \quad (3)$$

$$Y_C = 1 - \frac{\sum x.y_{C_xH_Y}.F_t}{F_{0,CH_4}} \quad (4)$$

where X_{CH4} is methane conversion, Y_{H2} is hydrogen yield, Y_C is carbon yield, and y_{CH4} and y_{H2} are methane and hydrogen mole fractions in the outlet stream, respectively. F_t is the outlet total molar flow rate (mol/min) and $F_{0,CH4}$ is the inlet molar flow rate of methane. y_{CxHy} is the outlet hydrocarbon

mole fraction while x and y are the carbon and hydrogen stoichiometry, respectively. The following hydrocarbons were considered: CH_4, C_2H_2, C_2H_4 and C_2H_6.

The outlet molar flow rate F_t, was calculated as follows:

$$F_t = \frac{F_{Ar}}{1 - y_{H_2} - \sum y_{C_xH_y}} \quad (5)$$

where F_{Ar} is the outlet molar flow rate of argon which is equal to its inlet rate $F_{0,Ar}$ (mol/min) since argon is inert.

The hydrostatic pressure of the melt was calculated as follows:

$$P = 10^{-2}.\rho\,.g\,.h \quad (6)$$

Where P is the hydrostatic pressure (mbar), ρ is the melt density (kg/m^3), g is the gravitational acceleration constant (9.81 m/s^2), and h is the melt height (m).

In a chemical reaction, the residence time of the chemical components in the reactional medium is a key parameter affecting conversion. Thus, it is essential to calculate the residence time to thoroughly analyze the results. In liquid tin, one should first estimate the bubble diameter to be able to calculate its rising velocity. The diameter of the bubble D_b (m) mainly depends on the inner radius of the feeder and some physical properties of the liquid phase. It can be estimated using Tate's law [18,34]:

$$D_b = \left(\frac{12\,R_0\,.\sigma}{(\rho_l - \rho_g)\,.g}\right)^{\frac{1}{3}} \quad (7)$$

where R_0 is the feeder inner radius (m), σ is the surface tension of the tin bath (N/m), ρ_l is the density of tin (kg/m^3), and ρ_g is the gas density (kg/m^3), which could be neglected compared to ρ_l.

Once the bubble diameter is estimated, the rising velocity v_b (m/s) of the bubble in liquid tin is calculated through an empirical equation [35]. Therefore, the residence time in the liquid phase τ_l (s) is the path distance (immersed height H_{im} (m)) divided by the rising velocity v_b:

$$\tau_l = \frac{H_{im}}{v_b} = \frac{H_{im}}{0.2969\,(D_b \times 10^2)^{0.316}} \quad (8)$$

On the other hand, the residence time of the gas in the headspace τ_g (s) can be directly calculated by dividing the effective volume of the reactor V_{eff} (the volume equivalent to the hot zone where there is a chemical reaction) by the thermally expanded inlet gas flow rate (CH_4 + Ar):

$$\tau_g = \frac{V_{eff}}{Q_0\,.\beta} = \frac{V_{eff}}{Q_0.\frac{P_0\,.\,(T + 273.15)}{P\,.(T_0 + 273.15)}} \quad (9)$$

where Q_0 is the inlet gas flow rate in normal conditions (Nm^3/s), β is the thermal expansion factor, P_0 is the normal atmospheric pressure (101 325 Pa), T_0 is the normal temperature (0 °C), and P and T are the operating conditions.

In long-run experiments, the theoretical value of carbon production was calculated as follows:

$$m_c = \sum_{t_0}^{t_{end}} \dot{F}_C.M_C = M_C.\sum_{t_0}^{t_{end}} (\dot{F}_{0,CH4} - \sum x.y_{C_xH_y}.\dot{F}_t) \quad (10)$$

where m_C is the total weight of produced carbon (g), t_0 and t_{end} are the starting and ending time of production (s), respectively, $\dot{F}_C$ is the molar flow rate of carbon (mol/s) and M_C is the molecular weight of carbon (12 g/mol).

In the experiment with steel particles, the bed void ratio or porosity (ε) was needed to obtain the total height of solid particles and liquid tin:

$$\varepsilon = \frac{V_v}{V_t} = 1 - \frac{V_{solid}}{V_t} = 1 - \frac{\rho_b}{\rho_s} \quad (11)$$

where V_v is the void volume (cm^3), V_t is the total volume occupied by the bed of steel particles (cm^3), V_{solid} is the net volume of solid in V_t, and ρ_b and ρ_s are the apparent density of the bed measured experimentally (particles + void) and the density of steel, respectively.

2.4.2 Parametric study

In order to study the impact of parameters such as temperature (1200-1300 °C), liquid height (immersed height of the feeder H_{im}=60-120-235 mm), inlet gas flow rate Q_0 (0.25-0.5 NL/min), and hybrid heating (electric heating vs. coupled electric/solar heating), a parametric study was achieved using the drilled tube (Figure 4). Nine runs were conducted in total with details summarized in Table 1. The first experimental series (runs #1 to #8) was conducted with a 120 mm tin bath with different immersed heights (Figure 4a&b). Then, a higher liquid height (≈ 235 mm) was considered (Figure 4c) to highlight its impact on methane pyrolysis in the bubble column. A higher liquid height means a longer path for bubbles in the liquid phase, which increases their space-time and improves methane decomposition.

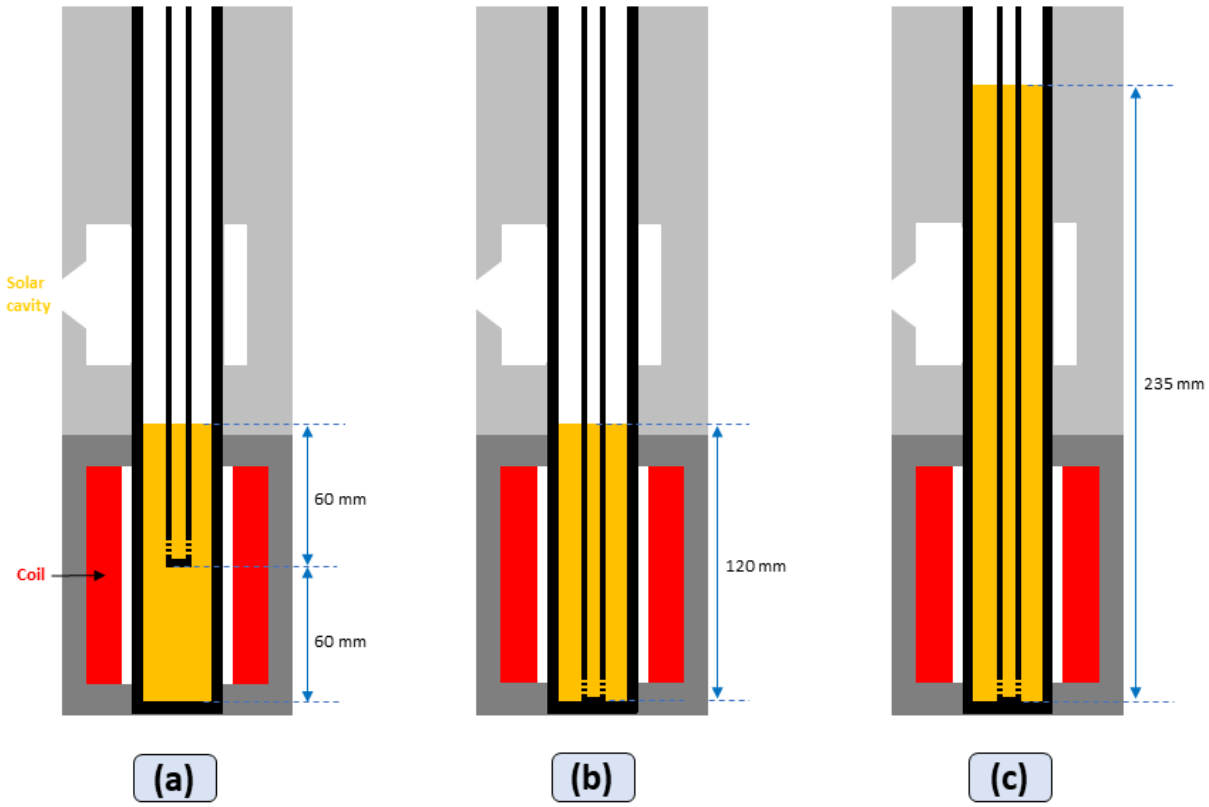

Figure 4: Reactor configurations for the parametric study. (a) immersed height = 60 mm, (b) immersed height = 120 mm, (c) immersed height = 235 mm

2.4.3 Addition of steel particles

Steel particles of small size (0.2-0.4 mm diameter) were added to the liquid tin bath (run #10). Steel has a density of 7.86 g/cm^3 which is higher than that of molten tin (6.47 g/cm^3 at 1100 °C). This ensures keeping the bed at the bottom around the feeder orifice and might help to generate small bubbles. 179 g of steel particles forming a bed of 100 mm height were inserted in the bottom of the reactor, then 308 g of tin granules (equivalent to a 120 mm tin bath) were added. An open-end feeder was used and both heating sources were activated because the tin surface was actually in the solar zone above the steel particles settled down. As steel particles melt in a temperature range of 1300-1550 °C [36] and corrosion with tin may occur, the heating temperature was kept safely below 1100 °C for a short period with conditions of run #10 given in Table 1.

2.4.4 Continuous runs for carbon separation assessment

To evaluate the stability of methane cracking in molten tin in terms of resistance against reactor clogging, two long-run experiments were conducted with different tube feeders (Table 1, runs #11 and #12). The height of the liquid phase was 120 mm at 1000 °C. Only electric heating was applied. Processing was continuous and no parameters were varied until complete clogging occurred (i.e., Q_0 and bath height were fixed). As the only exception, the temperature was raised to increase carbon production.

The aim of doing two experiments was to reproduce the results and to verify if the drilled tube could outperform the open-end tube.

Run #13 was a separate experiment, dedicated to verifying the possibility of a reverse reaction (Eq. (12)), especially in the less hot, upmost part of headspace. First, carbon production at the melt surface was required through first-step methane cracking with initial conditions in Table 1. The second step aimed to substitute methane flow rate with hydrogen while reducing the temperature of the headspace to just below 800 °C to check the possible reaction of carbon with hydrogen.

$$2H_{2(g)} + C_{(s)} \rightarrow CH_{4(g)} \qquad \Delta \mathrm{H^\circ}_{25\,^\circ\mathrm{C}} = -37.425\ \mathrm{kJ/mol\ of\ H_2} \tag{12}$$

Table 1: Operating conditions and results of methane cracking experiments in molten tin ($y_{0,CH4}$ = 0.3). Runs #1 to #9: parametric study, run #10: experiment with steel particles, runs #11 and #12: long-run experiments, run #13: experiment mainly dedicated to checking the possibility of any backward reaction (reverse of cracking)

Run #	Q_0 (NL/min)	H_{im} (mm)	T_{elec} (°C)	T_{solar} (°C)	Injector	y_{CH4}	y_{H2}	y_{C2H2}	y_{C2H4}	y_{C2H6}
1	0.5	60	1200	[800:850]	Drilled	0.28	0.02	2.95E-04	1.50E-03	5.53E-04
2	0.25	60	1200	[800:850]	Drilled	0.28	0.03	6.14E-04	1.88E-03	4.91E-04
3	0.25	120	1200	[800:850]	Drilled	0.24	0.07	1.34E-03	2.49E-03	5.26E-04
4	0.5	120	1200	[800:850]	Drilled	0.27	0.04	3.14E-03	3.36E-03	4.95E-04
5	0.25	120	1200	1200	Drilled	0.02	0.43	3.27E-03	2.15E-03	1.62E-04
6	0.25	120	1200	[800:850]	Drilled	0.19	0.16	4.04E-03	4.50E-03	2.89E-04
7	0.25	120	1300	[800:850]	Drilled	0.08	0.33	6.62E-03	3.27E-03	1.21E-04
8	0.5	120	1300	[800:850]	Drilled	0.14	0.24	7.78E-03	3.74E-03	1.28E-04
9	0.25	235	1200	1200	Drilled	0.12	0.28	5.47E-03	3.66E-03	1.41E-04
10	0.25	177	1100	1100	Open end + bed of steel particles (Φ = 0.2-0.4 mm)	0.16	0.19	3.00E-05	2.33E-03	3.11E-04
11 (long)	0.25	120	1300	[650:800]	Drilled	0.1-0.13	0.3-0.25	4.43E-03 to 7.05E-03	5.11E-03 to 3.60E-03	3.44E-04 to 1.29E-04
12 (long)	0.25	120	1300	[650:800]	Open end	0.1-0.13	0.3-0.26	8.70E-03 to 5.89E-03	3.47E-03 to 3.15E-03	1.56E-04 to 1.15E-04

13	0.25	120	1200	1200	Open end	0.05	0.38	5.73E-03	5.24E-03	3.26E-04

3 Results and discussion

3.1 Parametric study

Table 1 recaps the mole fractions of the outlet gases including H_2, unconverted CH_4, and secondary hydrocarbons (C_2H_2, C_2H_4, and C_2H_6). Q_0 in Table 1 represents the total inlet gas flow rate (composition: 70 mol% Ar and 30 mol% CH_4). Methane conversion, hydrogen and carbon yields are illustrated in Figure 5b. Temperature profiles of T_{solar} and T_{elec} are also shown (Figure 5a). In Figure 5b and under only electric heating (runs #1-2-3-4-6-7-8), the operating temperature in the x-axis was T_{elec}, with T_{solar} almost 800 °C. In contrast, under hybrid heating (runs #5 & #9), the operating temperature in the x-axis was the value of both T_{elec} and T_{solar}.

Under electric heating, T_{solar} was maintained between 800 °C and 850 °C to avoid any tin solidification if the liquid surface rises, especially at high gas flow rates (0.5 NL/min). Such a temperature was not high enough for any methane decomposition in the headspace (thermal methane decomposition starts at temperatures above 1000 °C) [12].

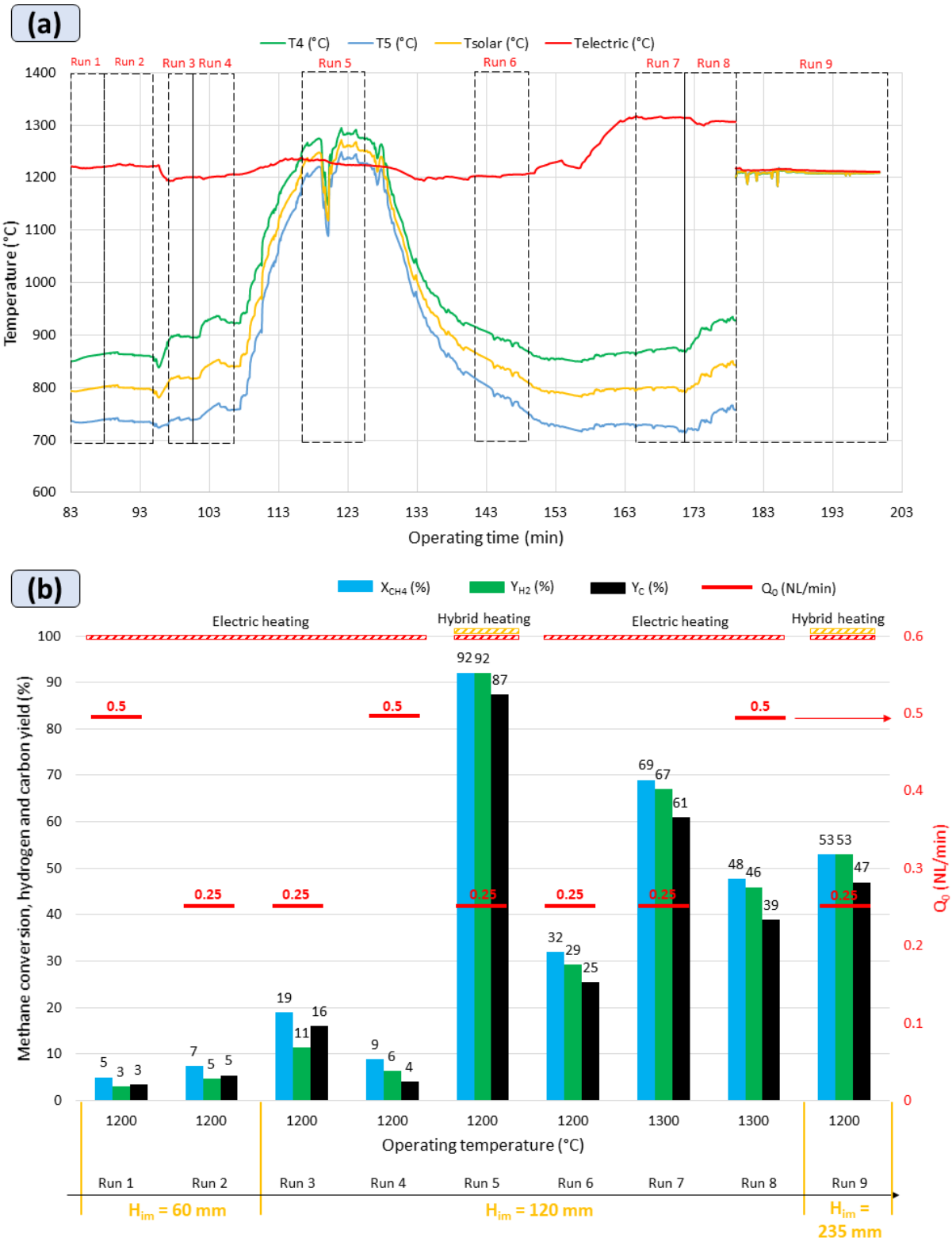

Figure 5: (a) Temperature profile, (b) Results of the parametric study

3.1.1 Effect of heating temperature

To unravel the temperature impact on methane decomposition, one should compare two identical runs with temperature as the only variable. For instance, runs #6 and #7 can be compared, where Q_0 was 0.25 NL/min and the feeder orifice completely immersed in the bath (H_{im} = 120 mm) under only

electric heating. Obviously, increasing the temperature from 1200 °C in run #6 to 1300 °C in run #7 improved methane conversion along with hydrogen and carbon yield from 32% to 69%, 29% to 67%, and 25% to 61%, respectively. Another explicit example could be runs #4 and #8, where there was only electric heating, a complete immersion (H_{im} = 120 mm) with Q_0 = 0.5 NL/min. Increasing T_{elec} from 1200 °C in run #4 to 1300 °C in run #8 boosted methane conversion (9% to 48%), hydrogen yield (6% to 46%), and carbon yield (4% to 39%). This conversion at 1300 °C in liquid tin (48%) is still lower than gas-phase pyrolysis (92%) at the same temperature [32]. However, the main advantage of methane pyrolysis in molten tin is the high resistance against clogging. In liquid media, the carbon floats atop the melt, unlike in gas phase where it likely sticks on the hot surfaces (reactor walls) thus hindering the process continuity [9].

Always in the context of the temperature effect, though both runs #3 & #6 were identical, the performance in run #6 was higher than in run #3 (X_{CH4} = 32% vs.19%, Y_{H2} = 29% vs. 11%, and Y_C = 25% vs. 16%). This result was most probably caused by the short post-effect of hybridization after run #5: the temperature of the gas phase above the melt remained above 820 °C (T_{solar}, run 3) by the time run #6 was launched. The temperature profiles in Figure 5a show that T4, T_{solar}, and T5 were still decreasing during run #6 (T_{solar} was almost 870 °C at the beginning of run #6) while they were stable during run #3 (T_{solar} ≈ 820 °C). Therefore, a part of the headspace, located just above the tin surface, was probably still hot enough to lead to some methane decomposition in gas phase.

This tendency of the effect of temperature in methane pyrolysis could be attributed to favorable thermodynamics. Since methane pyrolysis is endothermic (Eq (1)), providing more thermal energy shifts the reaction forward. Consequently, higher heating temperatures improve methane conversion and products yield.

3.1.2 Effect of liquid height H_{im}

In runs #2 & #3, Q_0 was 0.25 NL/min and there was only electric heating with T_{elec} = 1200 °C. In run #2, the feeder was half immersed (H_{im} = 60 mm), while there was complete immersion in run #3 (H_{im} = 120 mm). This difference in bath height led to higher methane conversion, hydrogen and carbon yields in run #3 as compared to run #2 (7% vs. 19%, 5% vs. 11%, and 5% vs. 16%, respectively). Based on Eq. (8), if H_{im} is doubled, the residence time is also doubled for a given bubble diameter.

Runs #1 & #4 were also identical with T_{elec} = 1200 °C and Q_0 = 0.5 NL/min, with H_{im} being the only variable. Again, the result showed increased performance when H_{im} was higher (120 mm). However, the improvement in methane conversion, hydrogen and carbon yields was less significant than that between runs #2 & #3 (X_{CH4} = 9% vs. 5%, Y_{H2} = 6% vs. 3%, and Y_C = 4% vs. 3% for run #4 and #1, respectively). Theoretically and according to Eq. (7), the diameter of bubbles does not depend on the gas flow rate, and hence the residence time of bubbles should be doubled in run #4 since H_{im} was increased from 60 mm to 120 mm (Eq. 8). However, Kulkarni et al. [37] reported that this is correct only in the single bubble regime. At low flow rates, the bubble diameter only depends on the orifice, the surface tension, and the density of the liquid phase. Once the flow rate is higher than a certain value, the regime changes to chain bubbling and the diameter of bubbles becomes directly proportional to the gas flow rate [37]. In this regime, the frequency of bubbles formation at the orifice is higher than their time of detachment from the feeder, which simply means that a formed bubble contains actually few single bubbles therein. Consequently, the bubbles are more likely to become bigger, which increases their rising velocity (the denominator in Eq. 8) and reduces their residence time.

3.1.3 Effect of residence time and medium type dependency

Another example of the effect of the liquid height could be illustrated by run #5 versus run #9. However, this comparison is critical because although there was hybrid heating in both runs and Q_0 was 0.25 NL/min (reducing the risk of inducing a chain bubbling regime), there was a fundamental difference in the gas path (as illustrated in Figure 6).

In run #5, the total residence time τ_5 could be split into τ_l, the residence time in the liquid phase (i.e., the first 120 mm of liquid tin) (Eq. (8)) and τ_g', the residence time of the gas in the headspace along the hot zone (up to 115 mm above the surface of the melt) (Eq. (9)). In run #9, there was only tin along the hot zone (235 mm of liquid tin), which homogenized the temperatures (overlaid plots in Figure 5a) and hence the residence time τ_9 was entirely related to the liquid phase. For analogy, τ_9 was also split into τ_l which was identical in both runs and τ_l', the residence time of bubbles in the upper 115 mm of liquid tin. Therefore, based on the scheme in Figure 6a, the main difference in the total residence time will be due to the difference between τ_l' and τ_g'.

Residence times in the liquid phase (τ_l and τ_l' in Figure 6b) were calculated in function of the bubble diameter to show their strong dependency. The residence time in the gas phase τ_g' was found constant (1.69 s) since it only depends on the effective volume of the reactor and the operating/initial conditions (T, P, Q_0).

The orifice of the drilled tube should theoretically have formed bubbles of 3.6 mm diameter (Eq. 7). For such bubbles, the total residence time in run #5 was more than twice that in run #9 (τ_5 = 2.25 s vs. τ_9 = 1.09 s). This was due to a much higher residence time in the gas phase (τ_g'=1.69 s) compared to that in liquid tin (τ_l'=0.53 s). Therefore, the type of the medium (liquid tin or gas) in the solar-heated zone (the upper 115 mm) had the major impact on the outstanding results in run #5 over run #9 (X_{CH4} = 92% vs. 53%, Y_{H2} = 92% vs. 53%, and Y_C = 87% vs. 47%). Gas phase pyrolysis outperforms liquid media pyrolysis in the present case for which bubbles are relatively large.

Figure 6b also shows that τ_9 could equalize τ_5 (3.45 s) only when the diameter of bubbles is around 0.1 mm. This is because such small bubbles equalize the residence time in the solar-heated zones (i.e., for D_b = 0.1 mm, τ_l' = τ_g' = 1.69 s). Moreover, with 0.1 mm bubbles, the overall gas-tin surface contact would be increased by a factor of 36 (ratio of the total surface of all bubbles). Briefly, small bubbles of this order of magnitude may drastically increase the residence time with improved heat and mass transfer and hence boost methane conversion. Configuration of run #9 also offers the possibility to run a round-the-clock hybrid process with solar heating during the day and electric heating at night.

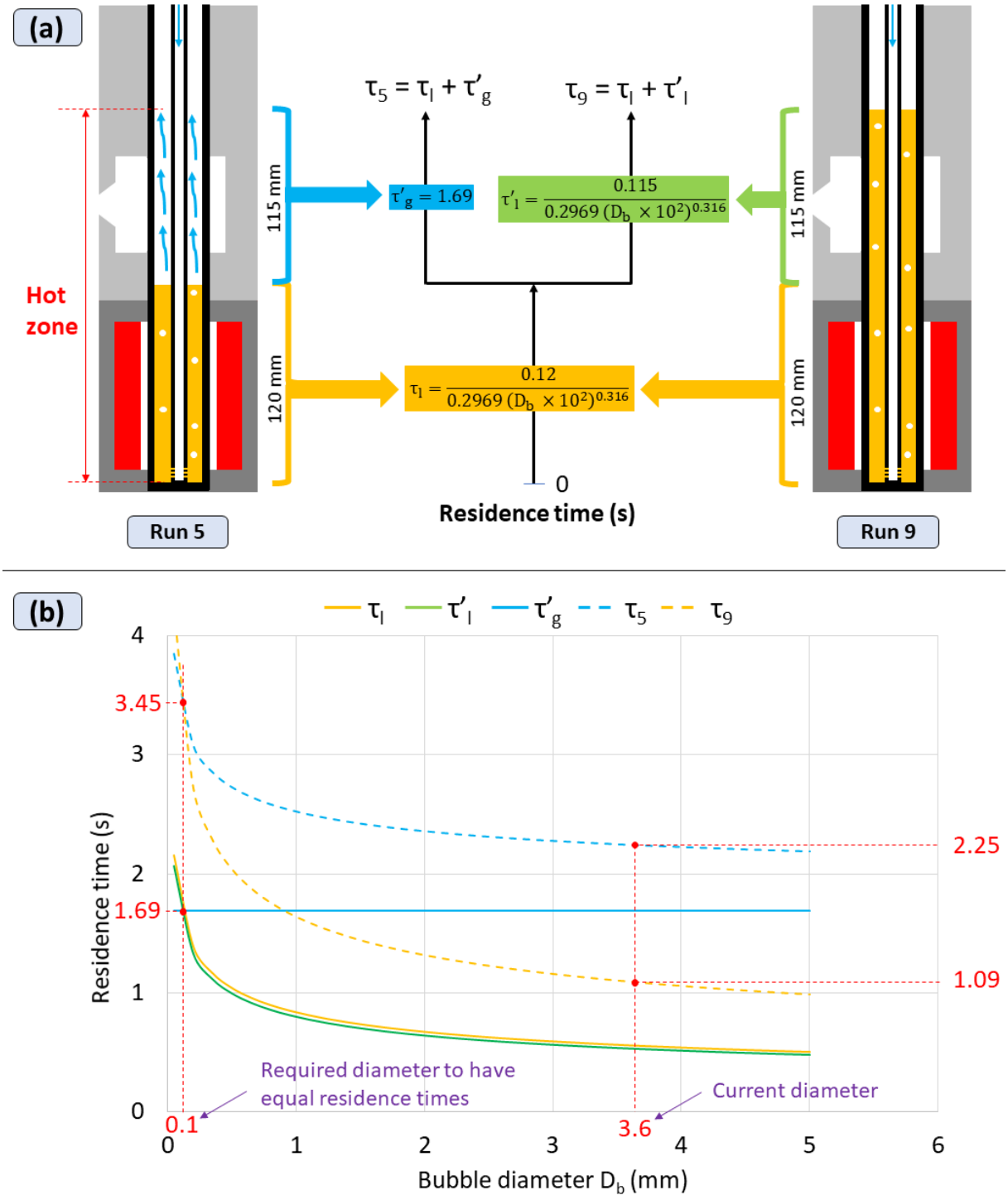

Figure 6: (a) Scheme representing the main difference of the gas path between run #5 & #9 with 120 mm and 235 mm liquid bath, respectively. (b) Residence time dependency on the diameter of bubbles

3.1.4 Effect of hybridization

Run #5 could be compared to run #3 where the only difference was the hybrid heating at 1200 °C. Clearly, the performance in run #5 was better (X_{CH4} = 92%, Y_{H2} = 92%, and Y_C = 87%). In this run, the 115 mm gas phase above the melt was heated by solar means to 1200 °C like the melt (run #5 in figure 5). Run #3 had the same configuration as run #5 except that the gas phase was not heated (T_{solar} = 800 °C, which is not high enough for methane decomposition). Thus, the residence time in run #5 was (τ_l+τ_g'=2.25 s, Figure 6,) vs. only (τ_l=0.56 s) in run #3, which explains this higher performance with hybrid heating. Hybrid heating in run #5 resulted in the best performance.

Finally, one could compare run #13 (open-end feeder) to run #5 (drilled feeder). The latter had better performance (X_{CH4} = 92% vs. 79%, Y_{H2} = 92% vs. 78%, and Y_C = 87% vs. 70%). Although the feeders were different, this could be mainly attributed to the higher temperature, especially $T_{solar} \approx 1250$ °C in run #5 (Figure 5), whereas it was very close to 1200 °C in run #13 (Figure 8). During the former, a cloud disturbed the DNI, which led T_{solar} to deviate from 1200 °C after stabilization. However, both runs still highlight the remarkable performance of the reactor under hybrid heating.

In summary, the higher the height of the heated zone, the longer the residence time and the better the pyrolysis performance.

3.2 Effect of steel particles bed addition

Knowing the apparent bed density (ρ_b = 4.45 g/cm^3) and the steel density (ρ_s = 7.86 g/cm^3), the void fraction in the 100 mm bed of steel particles was calculated using Eq. (11) (ε = 0.43). Consequently, considering a bed (100 mm) mixed with liquid tin (120 mm) inside the reactor, the overlaid melt was almost 177 mm high (bed + tin - void = 100 + 120 – 43 = 177 mm). Under hybrid heating, the hot zone is almost 235 mm high, which means that some cracking in gas phase may occur in the remaining 58 mm atop the melt.

The results of this experiment (run #10) revealed fairly good performance at a relatively low temperature of 1100 °C (X_{CH4} = 32%, Y_{H2} = 29%, and Y_C = 30%). However, this conversion was the result of partial conversions in both liquid and gas phases, although the former played an important role in the final result. Usually, methane cracking at 1100 °C is not significant, especially in liquid tin (≈0%) [32]. As tin constituted 75% of the hot zone (the rest being the gas phase), this conversion could not be attributed to the gas phase only. It is thus likely that the particles helped to increase the contact surface with gas and to reduce the diameter of the generated bubbles. With smaller generated bubbles, heat and mass transfer were boosted with an increased residence time in the liquid phase. Additional efforts are required to generate smaller bubbles but a fixed bed of small particles appears as a viable option.

One could notice the high carbon yield in run #10 (Y_C = 30%) compared to methane conversion (X_{CH4} = 32%). Moreover, the outlet molar fraction of C_2H_2 (3E-05) was very low compared to the other runs. Based on the most agreed mechanism of methane decomposition, especially in gas-phase, C_2H_2 is formed due to bonding of two CH* radicals [38]. This step is the latest before the formation of solid carbon with two hydrogen molecules. The fact that there was very little acetylene (C_2H_2) and high carbon yield suggests a different dissociation mechanism, mostly related to favored liquid-phase pyrolysis. The steel particles likely helped to generate small bubbles, which in turn increased the gas-liquid interfacial area, and hence favored methane decomposition at the surface of bubbles (liquid-phase pyrolysis).

3.3 Continuous experiments: process stability against clogging

Figure 7 shows the results of the long-run experiments performed with a tin bath of 120 mm and two different gas injectors (open-end and drilled tubes). Methane and hydrogen mole fractions in the outlet stream are plotted as a function of the operating time at three different temperatures (1200-1300-1400 °C) with fixed inlet gas flow rate and methane mole fraction (Q_0 = 0.25 NL/min and $y_{0,CH4}$ = 0.3). The pressure variations of the inlet (P_1) and outlet (P_2) of the reactor are also plotted to illustrate the process stability against clogging.

The atmospheric pressure in Odeillo is around 860 mbar. When the feeder was fully immersed, argon was injected (0.1 NL/min) and a hydrostatic pressure relevant to almost 110 mm of tin height (P_{hyd} = 70 mbar based on Eq. (6)) was added to P_1. This aspect could be clearly seen in the sudden increase

of P_1. For example, in case (a), P_1 increased to 940 mbar at t = 78 min and in case (b), it increased to 930 mbar at t = 56 min. For both experiments, temperature was stabilized at 1200 °C and methane was then injected, which additionally increased P_1 to almost 960 mbar (at t = 90 min and t = 96 min for case (a) and (b), respectively).

At 1200 °C, methane decomposition was poor in both cases: drilled feeder at t = 108 min (y_{CH4} = 0.25 and y_{H2} = 0.07 resulting in X_{CH4} = 14% and Y_{H2} = 12%) vs. open-end feeder at t = 124 min (y_{CH4} = 0.27 and y_{H2} = 0.05 resulting in X_{CH4} = 9% and Y_{H2} = 8%). Though the difference was not very high, the drilled feeder seemed to slightly enhance methane decomposition by enhancing hydrodynamics (smaller bubbles generation). It is possible that bubbles were not evenly generated by each of the nine holes of the drilled feeder, but only by some of them. This issue was observed in a transparent water column (although the injection area in both feeder designs (drilled and open-end) was equal, the pressure loss through the small drilled holes was not sufficient to ensure equal flow distribution between holes). In counterpart, less bubble-generating holes could raise the frequency of bubble generation and lead to more coalescence.

As these experiments were dedicated to investigating the process stability against clogging, the temperature was further increased to 1300 °C to enhance methane conversion and thus increase carbon production.

The temperature was stabilized at 1300 °C with the other conditions unchanged. The performance was further improved as expected, and almost identical methane conversions were obtained regardless of the feeder used: y_{CH4} = 0.1 and y_{H2} = 0.3 resulting in X_{CH4} = 61% and Y_{H2} = 60%, for the drilled (at t = 130 min) and open-end tube (at t = 147 min). The process was then held under these steady operating conditions to check how long the reactor could operate without clogging with P_1 and P_2 carefully monitored. Methane conversion was progressively and slowly decreasing over time in parallel with a slow increase of P_1. For example, in case (a) and after 3.7 h (at t = 345 min), P_1 reached 1020 mbar, y_{CH4} increased from 0.10 to 0.13, while y_{H2} decreased from 0.30 to 0.25 (X_{CH4} and Y_{H2} decreased from 61% to 50% and from 60% to 47%). In case (b) and after 2.2 h (at t =278 min), P_1 reached 966 mbar, y_{CH4} increased from 0.10 to 0.13, while y_{H2} decreased from 0.30 to 0.26 (X_{CH4} and Y_{H2} decreased from 61% to 51% and from 60% to 49%).

It was clear in both cases that the reactor withstood well against clogging with P_1 increasing very slowly (due to carbon accumulation at the melt surface) while P_2 remained stable. For this reason, the temperature was finally increased to 1400 °C to assess stability under higher temperatures yielding higher carbon production rates and conversions. In case (a), y_{CH4} decreased to 0.04 and y_{H2} increased to 0.39 resulting in X_{CH4} = 83% and Y_{H2} = 82%. In case (b), y_{CH4} decreased to 0.037 and y_{H2} increased to 0.40 resulting in X_{CH4} = 84% and Y_{H2} = 83%. P_1 had been rising progressively until it drastically reached 1676 mbar and 1100 mbar in case (a) and case (b), respectively. Thus, methane injection was stopped. This dramatic increase of P_1 at 1400 °C pointed out an early methane pyrolysis in the inner tube, clogging the orifice of the feeder.

Using Eq. (10), the total theoretical weight of produced carbon was calculated. Experimentally, carbon was mainly found in the reactor at the melt surface, which means that only small amounts of carbon were entrained by the outlet gas toward the cartridge gas filters. The overall mass of the reactor and filters was weighed before and after experiments, which allowed to deduce the net mass of produced carbon accurately, knowing the initial mass of tin. In case (a), the total carbon produced $m_{a\text{-theoretical}}$ was 6 g while the experimental amount was 5.15 g, which is a good fit. In case (b), $m_{b\text{-theoretical}}$ was 4.15 g vs. 4 g obtained experimentally.

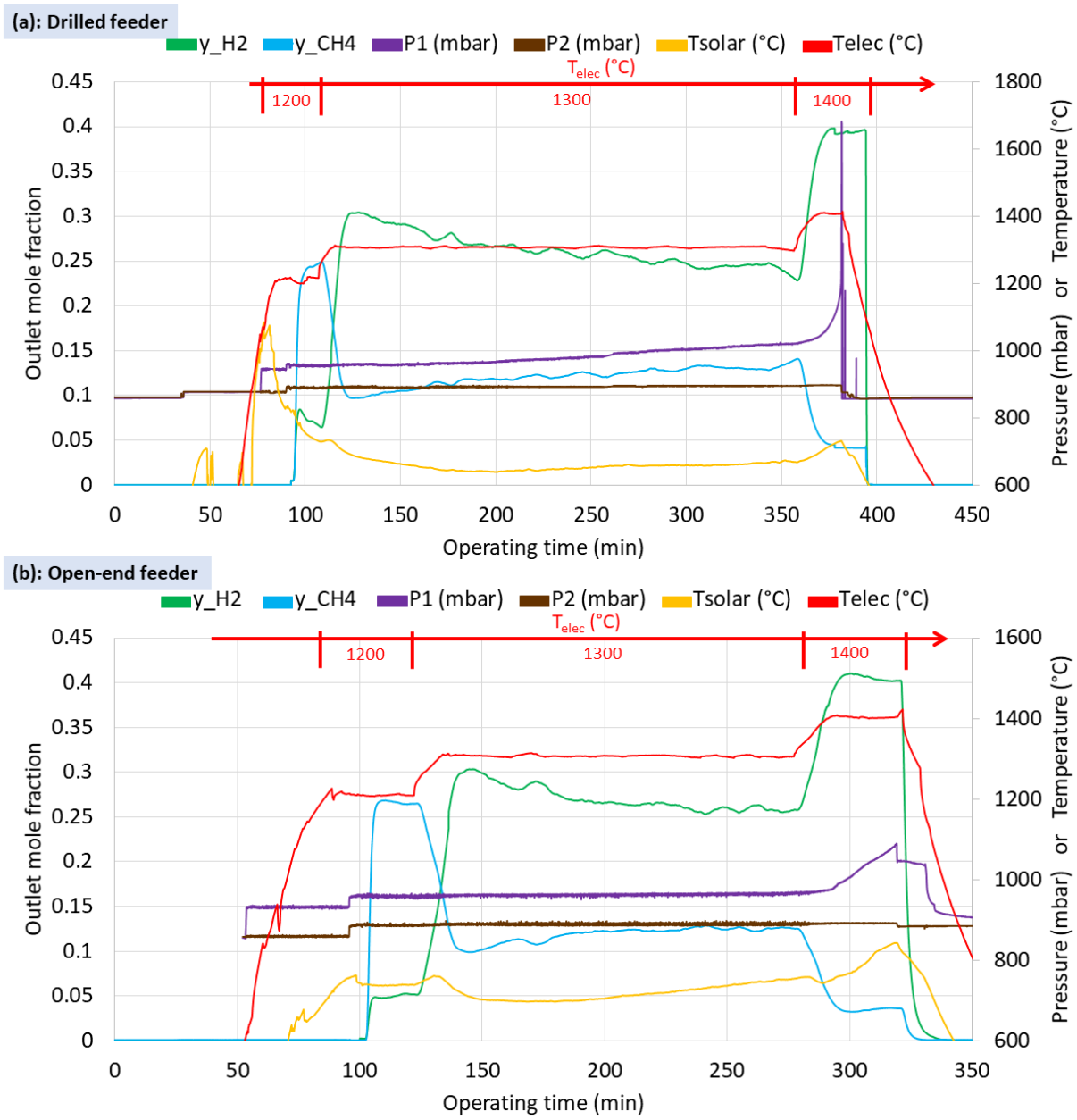

Figure 7: Methane and hydrogen outlet mole fractions as well as temperature and pressure variations as a function of time in the long-run experiments: (a) drilled feeder, (b) open-end feeder

The slight continuous decrease in methane conversion during the long-run experiments was discussed. A two-step experiment (Figure 8) was carried out to check the possibility of reversed recombination reaction between carbon and hydrogen in the headspace region above the melt where the temperature is lower than that of the tin bath (Eq. 12). First, carbon was produced at the melt surface and then methane flow was substituted by hydrogen. The first step was run #13, which was exactly the same as run #5 with an open-end feeder instead (Q_0 = 0.25 NL/min, H_{im} = 120 mm, T_{solar} and T_{elec} were both 1200 °C). Electric heating was then held at 1200 °C while solar heating was stopped to reduce the temperature of the headspace (600<T_{solar}<800 °C). Methane flow was substituted by hydrogen (Q_0 = 0.25 NL/min, $y_{0,H2}$ = 0.3).

In the first step (run #13) at t = 100 min, y_{H2} reached 0.38 with y_{CH4} around 0.06 (X_{CH4} = 79%, Y_{H2} = 78% and Y_C = 70%). At equilibrium (120<t<150 min), y_{H2} was about 0.35 and y_{CH4} was 0.07 (X_{CH4} = 72%, Y_{H2} = 71% and Y_C = 69%). During the first step, 3 g of carbon were produced overall with only 0.4 g

captured in the first cartridge filter (based on Eq. (10), $m_{theoretical}$ = 3.15 g). In the second step, the test was run for almost 20 min (t =188-208 min). The results showed a constant outlet hydrogen mole fraction equal to that of the inlet (y_{H2} = 0.3) with zero methane production. Consequently, no backward reaction took place in the headspace even in its upmost parts where the temperature was even much lower than T_{solar}.

As the reverse reaction hypothesis was excluded, other explanations could help to understand the dropping behavior of methane conversion. Firstly, with continuous processing, carbon accumulates on the surface of the melt, which gradually reduces the headspace (147 cm^3) and thus the residence time in gas phase. This result may diminish the conversion in the hot headspace above the melt. Secondly, while methane was decomposing, the pressure difference between P_1 and P_2 was gradually rising, which might have increased gas velocity. An increased gas velocity could cause a reduction of the gas residence time. Such a tendency results in a gradual drop in methane conversion.

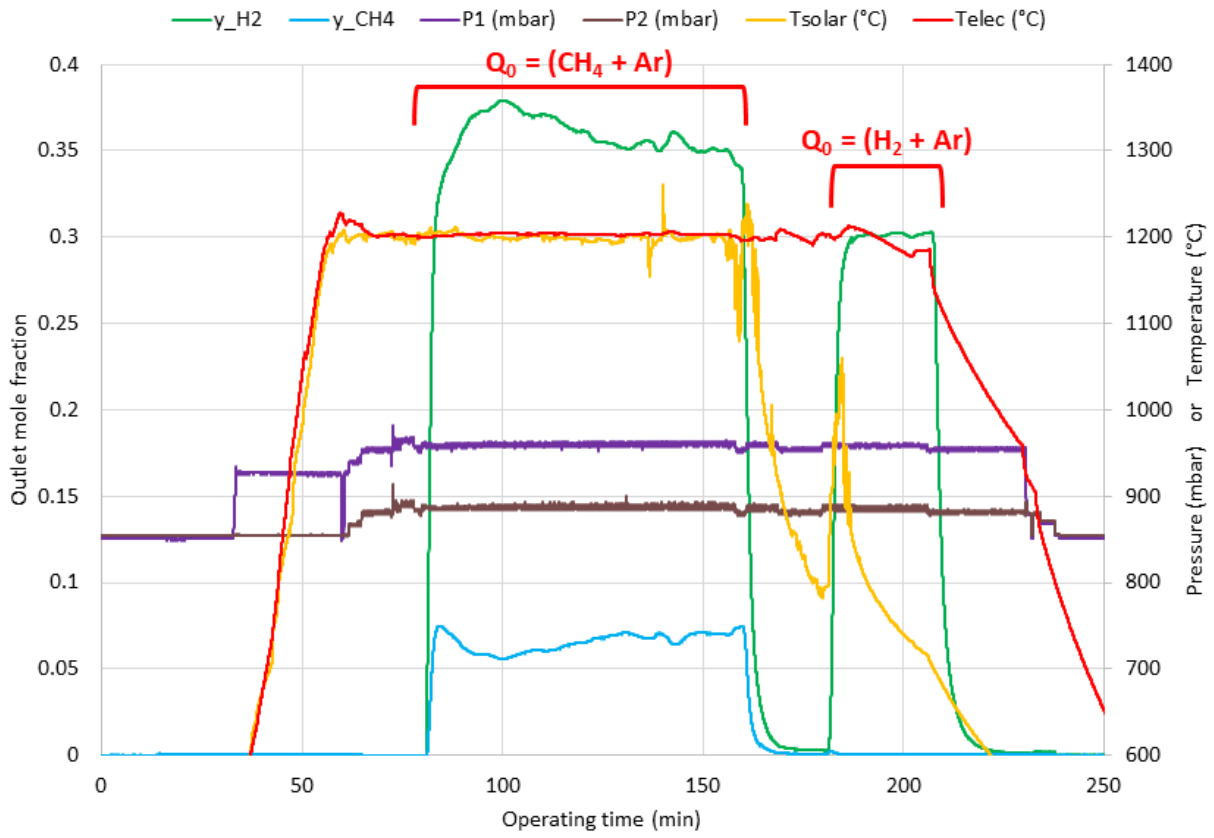

Figure 8: Results of a two-step experiment to verify the possibility of a reverse reaction in the headspace (Eq. (12)).

3.4 Carbon product characterization

Carbon samples accumulated at the melt surface were collected from the outer tube of the reactor in the long-run experiments and were characterized.

3.4.1 Morphology and elemental composition analysis

Scanning electron microscopy (SEM, HITACHI S4800) was used to analyze the morphology of carbon specimens (Figure 9) Noticeably, all of the collected carbons show a sheet-like structure, frequently encountered during methane pyrolysis in molten media [24,26,32]. Such sheets were most probably formed during the breakage of bubbles at the melt surface. During methane decomposition in bubbles, the carbon is formed at the gas-liquid interface as spherical sheets. Once bubbles reach the melt surface, they break up to leave carbon sheets floating above.

Energy dispersive X-Ray spectroscopy (EDX, Oxford Instruments X-Max N SDD) was used to determine the chemical composition of the carbon samples. Figure 10 shows different selected spectra, and Table 2 recaps their chemical composition. Three chemical elements were found almost in every spectrum (C, Sn, and O). Tin was shown in Figure 10 as white spots. Although EDX is semi-quantitative, it helped to confirm tin contamination in the carbon samples, as it provides a global elemental composition depending on the analysis area. The presence of tin was highly expected due to possible tin entrainment to the floating carbon followed by solidification. For example, with the drilled feeder, the highest tin content was in spectrum 22 scanning a tin particle (82.28 wt%). With the open-end feeder, spectrum 18 had the highest tin content (44.11 wt%). Globally when scanning larger zones, tin content was much lower (7.56 wt% in spectrum 20 and 3.62 wt% in spectrum 14 with the drilled and open-end feeders, respectively). Oxygen presence was mostly due to the oxidation of tin. Although the reactor was initially purged with argon and the startup and shutdown steps were achieved quickly, some oxidation of tin may have occurred. EDX mapping illustrates the distribution of C, Sn, and O (Figure 11). Carbon is the most dominant, while Sn and O are also spread through the total surface of the sample.

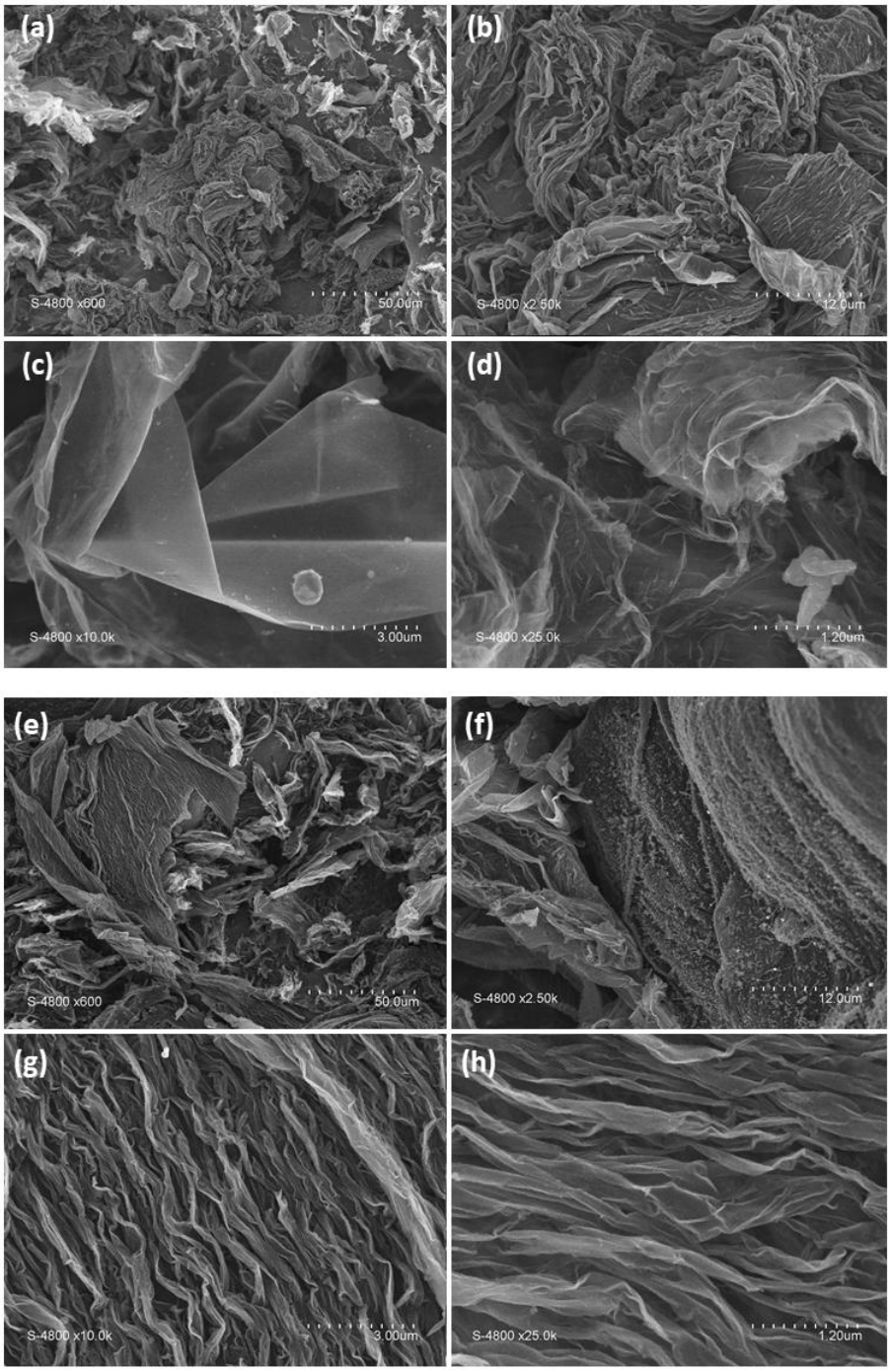

Figure 9: SEM images of the carbon samples recovered from the outer tube with progressive zooming. Drilled feeder: (a), (b), (c) and (d), open-end feeder: (e), (f), (g) and (h).

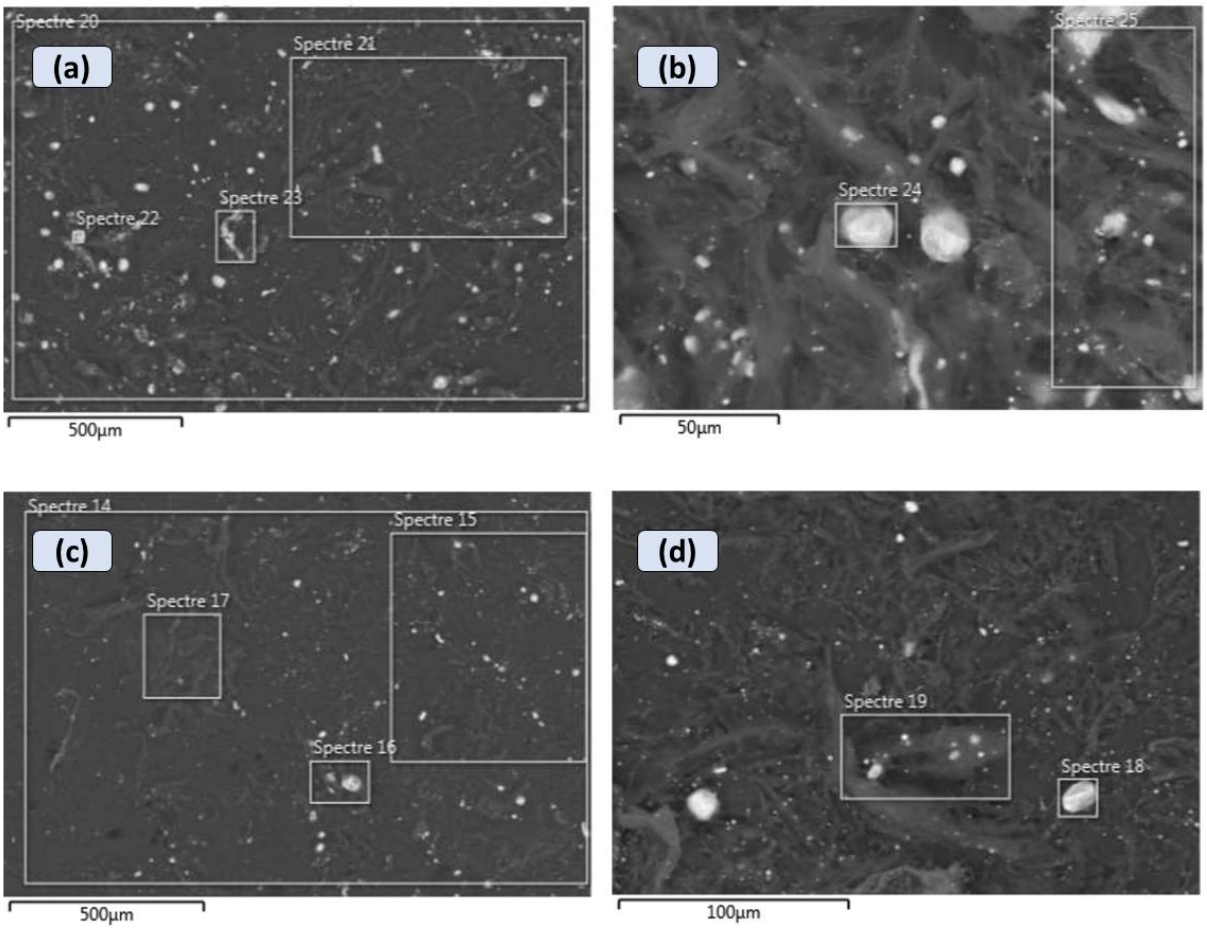

Figure 10: Electronic images and selected spectrum zones for carbon samples of long-run experiments. (a) and (b) drilled feeder, (c) and (d) open-end feeder.

Table 2: Chemical composition data from EDX relevant to spectra of Figure 10

	Spectrum N°	**C (wt%)**	**O (wt%)**	**Sn (wt%)**	**Total (wt%)**
Drilled feeder	20	81.77	10.67	7.56	100
	21	83.96	9.01	7.02	99.99
	22	17.72	0	82.28	100
	23	69.07	6.56	24.37	100
	24	39.99	2.09	57.92	100
	25	80.4	7.38	12.21	99.99
Open-end feeder	14	81.06	15.32	3.62	100
	15	80.27	15.26	4.47	100
	16	75.4	5.96	18.64	100
	17	86.25	9.99	3.76	100
	18	48.05	7.85	44.11	100.01

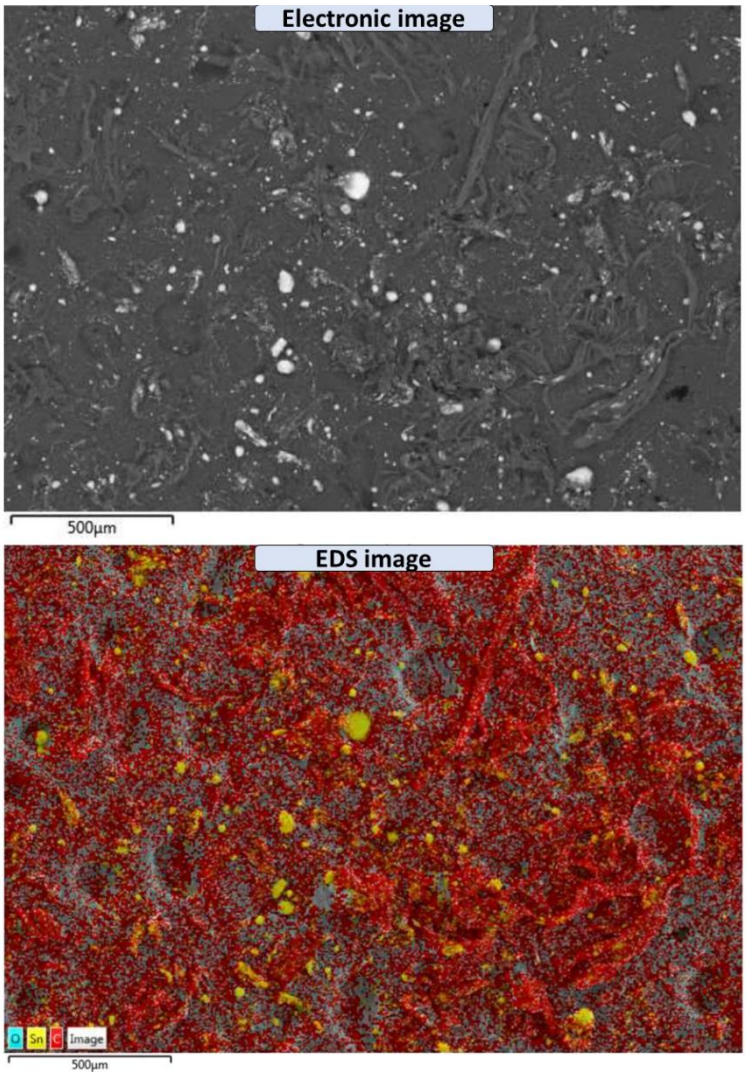

Figure 11: Electronic image with its EDX mapping below. (Carbon specimen from the long-run experiment with the drilled feeder)

3.4.2 X-ray diffraction analysis

X-ray diffraction (XRD: Malvern Panalytical X'Pert PRO) was also used for structural analysis of carbon and species identification. The results for both long-run experiments were very similar (Figure 12a&b). The peaks reveal the presence of graphitic carbon, whose formation is common in liquid-phase methane pyrolysis [20,24,26,32,39]. Using Scherrer equation [32], the average crystallite size was about 3 nm in both samples. Tin presence was also evidenced through XRD, confirming a tin-contaminated carbon. Traces of SnO_2 was also identified, which corroborates the oxygen presence in EDX analysis. Apparently, some oxidation took place, most probably during the startup and shutdown steps or sample recovery.

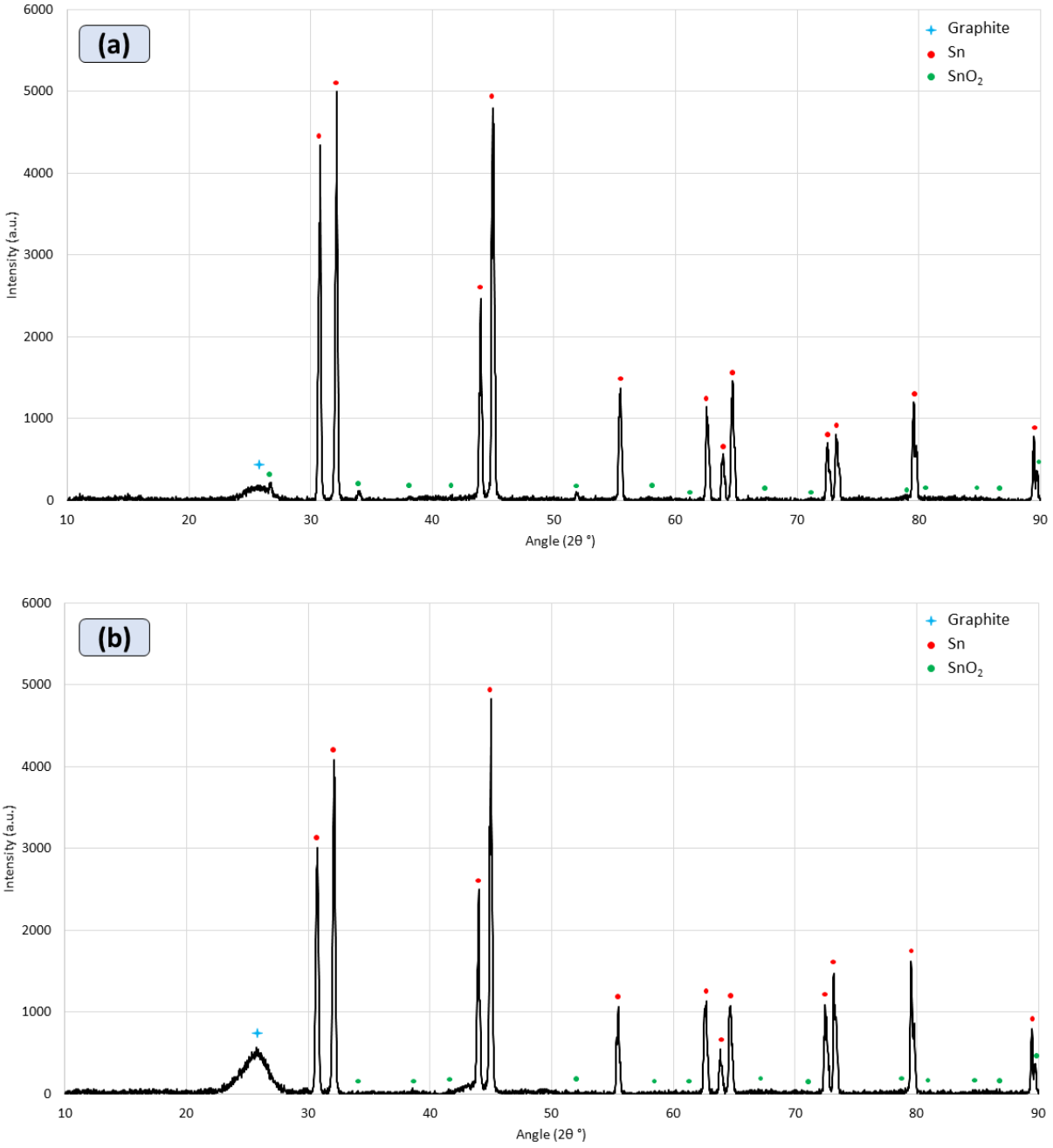

Figure 12: XRD for carbon samples from the reactor in the long-run experiments: (a) case of the drilled feeder, (b) case of the open-end feeder.

4 Conclusions

Methane cracking for hydrogen production (namely turquoise H_2) could be an alternative path with zero greenhouse gas emissions. However, such a process still needs thorough investigation, especially in its newest approach known as pyrolysis in molten media. Challenges mainly consist in finding a relevant catalytic liquid medium and improving the hydrodynamics of bubbles to boost methane decomposition. The methane pyrolysis in molten tin was experimentally studied in a novel hybrid solar/electric bubbling reactor. This study revealed the effect of several parameters on methane decomposition and key findings are summarized below.

- The heating temperature was a key factor to enhance the performance. For instance, increasing the temperature of the electric heater from 1200 °C to 1300 °C with constant Q_0 (0.25 NL/min) and melt height (H_{im} = 120 mm) improved methane conversion along with hydrogen and carbon yield from 32% to 69%, 29% to 67%, and 25% to 61%, respectively.
- The inlet flow rate increase hinders methane conversion. Tate's law shows that the inlet flow rate does not directly affect the size or the velocity of the bubbles in the single bubbling regime. However, higher flow rates shift the single bubbling regime toward chain bubbling regime or slug flow, which decreases residence time and limits heat and mass transfer (thus reducing methane conversion) due to coalescence. For example, increasing Q_0 from 0.25 to 0.5 NL/min at constant temperature (T_{elec} = 1200 °C) and melt height (H_{im} = 120 mm) led to a decrease in methane conversion from 19% to 9%.
- Hybridization had great influence on methane pyrolysis. When solar and electric heating were simultaneously activated, the hot zone was enlarged. Thus, the residence time of the gas was increased, which boosted methane conversion (X_{CH4} increased from 19% to 92% at constant Q_0 (0.25 NL/min) and melt height (H_{im} = 120 mm)).
- The impact of the size of the bubbles was addressed. Generating small bubbles is very important to improve heat and mass transfer and residence time. For instance, during hybridization, it was shown that the residence time of methane in a gas phase of 115 mm height is much higher than that of bubbles (D_b = 3.6 mm) in a similar height of liquid tin (1.69 s vs. 0.53 s). To equalize the residence time, the diameter of the bubbles should be smaller than 0.1 mm. The drilled tube was not efficient to evenly generate small bubbles probably because of too large holes. A 100 mm high bed of steel particles helped to increase the contact surface with gas, which resulted in a significant conversion (32%) at a relatively low temperature (1100 °C).
- The continuity of the process was evidenced through two similar long-run experiments with the feeder orifice as the only difference. In short, the process was very stable at temperatures up to 1300 °C for more than 3.7 h (drilled feeder) and 2.2 h (open-end feeder) for each. The process could have lasted much longer if the temperature had not been increased to 1400 °C for which the kinetics became very high and early methane conversion took place in the injector, which resulted in clogging in the injector (gas-phase pyrolysis).
- The carbon co-product recovered at the melt surface was analyzed and a sheet-like structure was observed.

This study proved continuous carbon separation without clogging as one of the main advantages of pyrolysis in molten media. Other aspects such as finding a suitable catalytic liquid medium or generating small bubbles via suitable spargers are still a challenge to further improve the efficiency of this new pathway for clean hydrogen production.

Acknowledgments

The authors thank Roger Garcia (PROMES-CNRS) for his support in the design and installation of the solar reactor, Régis Rodriguez and Emmanuel Guillot for their support to set the data acquisition system, and Eric Bêche for XRD analysis.

Funding

This work was partially supported by the French ''Investments for the future" program managed by the National Agency for Research, under contract ANR-10-LABX-22-01 (Labex SOLSTICE).

Author Contributions:

Methodology, Validation, Formal analysis, Investigation, Data curation, M.M., S.R., and S.A.; Writing—original draft preparation, M.M.; writing—review and editing, M.M., S.R., and S.A.; supervision, S.R. and S.A.; project administration, S.R. and S.A.; funding acquisition, S.R. and S.A. All authors have read and agreed to the published version of the manuscript.

References

[1] Hydrogen 2020. https://www.iea.org/fuels-and-technologies/hydrogen (accessed January 13, 2022).

[2] Curcio A, Rodat S, Vuillerme V, Abanades S. Experimental assessment of woody biomass gasification in a hybridized solar powered reactor featuring direct and indirect heating modes. Int J Hydrogen Energy 2021;46:37192–207. https://doi.org/10.1016/j.ijhydene.2021.09.008.

[3] Dagle RA, Dagle V, Bearden MD, Holladay JD, Krause TR, Ahmed S. An Overview of Natural Gas Conversion Technologies for Co-Production of Hydrogen and Value-Added Solid Carbon Products. Pacific Northwest National Lab: Richland, WA, USA, WA (United States): 2017. https://doi.org/10.2172/1411934.

[4] Pinilla JL, Utrilla R, Karn RK, Suelves I, Lázaro MJ, Moliner R, et al. High temperature iron-based catalysts for hydrogen and nanostructured carbon production by methane decomposition. Int J Hydrogen Energy 2011;36:7832–43. https://doi.org/10.1016/j.ijhydene.2011.01.184.

[5] Echegoyen Y, Suelves I, Lázaro MJ, Moliner R, Palacios JM. Hydrogen production by thermocatalytic decomposition of methane over Ni-Al and Ni-Cu-Al catalysts: Effect of calcination temperature. J Power Sources 2007;169:150–7. https://doi.org/10.1016/j.jpowsour.2007.01.058.

[6] Ashik UPM, Wan Daud WMA, Abbas HF. Production of greenhouse gas free hydrogen by thermocatalytic decomposition of methane - A review. Renew Sustain Energy Rev 2015;44:221–56. https://doi.org/10.1016/j.rser.2014.12.025.

[7] Utrilla R, Pinilla JL, Suelves I, Lázaro MJ, Moliner R. Catalytic decomposition of methane for the simultaneous co-production of CO2-free hydrogen and carbon nanofibre based polymers. Fuel 2011;90:430–2. https://doi.org/10.1016/j.fuel.2010.08.004.

[8] Rodat S, Abanades S, Coulié J, Flamant G. Kinetic modelling of methane decomposition in a tubular solar reactor. Chem Eng J 2009;146:120–7. https://doi.org/10.1016/j.cej.2008.09.008.

[9] Abánades A, Ruiz E, Ferruelo EM, Hernández F, Cabanillas A, Martínez-Val JM, et al. Experimental analysis of direct thermal methane cracking. Int J Hydrogen Energy 2011;36:12877–86. https://doi.org/10.1016/j.ijhydene.2011.07.081.

[10] MURADOV N. How to produce hydrogen from fossil fuels without CO2 emission. Int J Hydrogen Energy 1993;18:211–5. https://doi.org/10.1016/0360-3199(93)90021-2.

[11] Suelves I, Lázaro MJ, Moliner R, Pinilla JL, Cubero H. Hydrogen production by methane decarbonization: Carbonaceous catalysts. Int J Hydrogen Energy 2007;32:3320–6. https://doi.org/10.1016/j.ijhydene.2007.05.028.

[12] Msheik M, Rodat S, Abanades S. Methane Cracking for Hydrogen Production: A Review of Catalytic and Molten Media Pyrolysis. Energies 2021;14:3107. https://doi.org/10.3390/en14113107.

[13] Tyrer D. “Production of hydrogen” U.S. Patent 1 803 221, Apr. 28,. The United States Patent

Office. 1803221, 1931. https://doi.org/10.1126/science.53.1377.481.

[14] Jafarian M, Abdollahi MR, Nathan GJ. Preliminary evaluation of a novel solar bubble receiver for heating a gas. Sol Energy 2019;182:264–77. https://doi.org/10.1016/j.solener.2019.02.027.

[15] Zeng J, Tarazkar M, Pennebaker T, Gordon MJ, Metiu H, McFarland EW. Catalytic Methane Pyrolysis with Liquid and Vapor Phase Tellurium. ACS Catal 2020;10:8223–30. https://doi.org/10.1021/acscatal.0c00805.

[16] Leal Pérez BJ, Medrano Jiménez JA, Bhardwaj R, Goetheer E, van Sint Annaland M, Gallucci F. Methane pyrolysis in a molten gallium bubble column reactor for sustainable hydrogen production: Proof of concept & techno-economic assessment. Int J Hydrogen Energy 2020. https://doi.org/10.1016/j.ijhydene.2020.11.079.

[17] Wang K, Li WS, Zhou XP. Hydrogen generation by direct decomposition of hydrocarbons over molten magnesium. J Mol Catal A Chem 2008;283:153–7. https://doi.org/10.1016/j.molcata.2007.12.018.

[18] Zaghloul N, Kodama S, Sekiguchi H. Hydrogen Production by Methane Pyrolysis in a Molten-Metal Bubble Column. Chem Eng Technol 2021;44:1986–93. https://doi.org/10.1002/ceat.202100210.

[19] Plevan M, Geißler T, Abánades A, Mehravaran K, Rathnam RK, Rubbia C, et al. Thermal cracking of methane in a liquid metal bubble column reactor: Experiments and kinetic analysis. Int J Hydrogen Energy 2015;40:8020–33. https://doi.org/10.1016/j.ijhydene.2015.04.062.

[20] Serban M, Lewis MA, Marshall CL, Doctor RD. Hydrogen production by direct contact pyrolysis of natural gas. Energy and Fuels 2003;17:705–13. https://doi.org/10.1021/ef020271q.

[21] Geißler T, Plevan M, Abánades A, Heinzel A, Mehravaran K, Rathnam RK, et al. Experimental investigation and thermo-chemical modeling of methane pyrolysis in a liquid metal bubble column reactor with a packed bed. Int J Hydrogen Energy 2015;40:14134–46. https://doi.org/10.1016/j.ijhydene.2015.08.102.

[22] Kim J, Oh C, Oh H, Lee Y, Seo H, Kim YK. Catalytic methane pyrolysis for simultaneous production of hydrogen and graphitic carbon using a ceramic sparger in a molten NiSn alloy. Carbon N Y 2023;207:1–12. https://doi.org/10.1016/j.carbon.2023.02.053.

[23] Scheiblehner D, Neuschitzer D, Wibner S, Sprung A, Antrekowitsch H. Hydrogen production by methane pyrolysis in molten binary copper alloys. Int J Hydrogen Energy 2023;48:6233–43. https://doi.org/10.1016/j.ijhydene.2022.08.115.

[24] Kang D, Rahimi N, Gordon MJ, Metiu H, McFarland EW. Catalytic methane pyrolysis in molten MnCl2-KCl. Appl Catal B Environ 2019;254:659–66. https://doi.org/10.1016/j.apcatb.2019.05.026.

[25] Bae D, Kim Y, Ko EH, Ju Han S, Lee JW, Kim M, et al. Methane pyrolysis and carbon formation mechanisms in molten manganese chloride mixtures. Appl Energy 2023;336:120810. https://doi.org/10.1016/j.apenergy.2023.120810.

[26] Rahimi N, Kang D, Gelinas J, Menon A, Gordon MJ, Metiu H, et al. Solid carbon production and recovery from high temperature methane pyrolysis in bubble columns containing molten metals and molten salts. Carbon N Y 2019;151:181–91. https://doi.org/10.1016/j.carbon.2019.05.041.

[27] Patzschke CF, Parkinson B, Willis JJ, Nandi P, Love AM, Raman S, et al. Co-Mn catalysts for H 2 production via methane pyrolysis in molten salts. Chem Eng J 2021;414:128730. https://doi.org/10.1016/j.cej.2021.128730.

[28] Pan Y, Lo V, Cao L, Roy A, Chivers B, Noorbehesht N, et al. Graphitic carbon from catalytic methane decomposition as efficient conductive additives for zinc-carbon batteries. Carbon N Y 2022;192:84–92. https://doi.org/10.1016/j.carbon.2022.02.049.

[29] Carbon Black Market - Growth, Trends, COVID-19 Impact, and Forecasts (2022 - 2027) n.d. https://www.mordorintelligence.com/industry-reports/carbon-black-market (accessed January 28, 2022).

[30] Kudinov IV, Pimenov AA, Kryukov YA, Mikheeva GV. A theoretical and experimental study on hydrodynamics, heat exchange and diffusion during methane pyrolysis in a layer of molten tin. Int J Hydrogen Energy 2021. https://doi.org/10.1016/j.ijhydene.2020.12.138.

[31] Von Wald GA, Masnadi MS, Upham DC, Brandt AR. Optimization-based technoeconomic analysis of molten-media methane pyrolysis for reducing industrial sector CO 2 emissions. Sustain Energy Fuels 2020;4:4598–613. https://doi.org/10.1039/D0SE00427H.

[32] Msheik M, Rodat S, Abanades S. Experimental comparison of solar methane pyrolysis in gas-phase and molten-tin bubbling tubular reactors. Energy 2022;260:124943. https://doi.org/10.1016/j.energy.2022.124943.

[33] Alchagirov BB, Chochaeva AM. Temperature dependence of the density of liquid tin. High Temp 2000;38:44–8. https://doi.org/10.1007/BF02755565.

[34] Paxman D, Trottier S, Nikoo M, Secanell M, Ordorica-Garcia G. Initial experimental and theoretical investigation of solar molten media methane cracking for hydrogen production. Energy Procedia 2014;49:2027–36. https://doi.org/10.1016/j.egypro.2014.03.215.

[35] Andreini RJ, Foster JS, Callen RW. Characterization of gas bubbles injected into molten metals under laminar flow conditions. Metall Trans B 1977;8:625–31. https://doi.org/10.1007/BF02669340.

[36] Won YM, Kim K, Yeo T, Oh KH. Effect of Cooling Rate on ZST, LIT and ZDT of Carbon Steels Near Melting Point. ISIJ Int 1998;38:1093–9. https://doi.org/10.2355/isijinternational.38.1093.

[37] Kulkarni AA, Joshi JB. Bubble Formation and Bubble Rise Velocity in Gas−Liquid Systems: A Review. Ind Eng Chem Res 2005;44:5873–931. https://doi.org/10.1021/ie049131p.

[38] Sánchez-Bastardo N, Schlögl R, Ruland H. Methane Pyrolysis for CO2-Free H2 Production: A Green Process to Overcome Renewable Energies Unsteadiness. Chemie-Ingenieur-Technik 2020;92:1596–609. https://doi.org/10.1002/cite.202000029.

[39] Kang D, Palmer C, Mannini D, Rahimi N, Gordon MJ, Metiu H, et al. Catalytic Methane Pyrolysis in Molten Alkali Chloride Salts Containing Iron. ACS Catal 2020;10:7032–42. https://doi.org/10.1021/acscatal.0c01262.